Collective locomotion of two self-propelled flapping plates with different propulsive capacities

Ze-Rui Peng, Haibo Huang, and Xi-Yun Lu

Citation: Physics of Fluids **30**, 111901 (2018); doi: 10.1063/1.5053662
View online: https://doi.org/10.1063/1.5053662
View Table of Contents: http://aip.scitation.org/toc/phf/30/11
Published by the American Institute of Physics

PHYSICS TODAY
WHITEPAPERS
ADVANCED LIGHT CURE ADHESIVES
Take a closer look at what these environmentally friendly adhesive systems can do
READ NOW
PRESENTED BY
MASTERBOND
ADHESIVES | SEALANTS | COATINGS

Collective locomotion of two self-propelled flapping plates with different propulsive capacities

Ze-Rui Peng, Haibo Huang,[a)] and Xi-Yun Lu
Department of Modern Mechanics, University of Science and Technology of China, Hefei 230026, China

(Received 24 August 2018; accepted 1 November 2018; published online 29 November 2018)

The role of the hydrodynamic effect in the collective locomotion of several birds or fish is an interesting topic. Taking a model of a self-propelled flapping plate, we numerically investigated the collective locomotion of a pair of plates with comparable but different propulsive capacities, e.g., one long and one short plates. The longer plate is supposed to have a stronger propulsive capacity. It is found that two typical equilibrium configurations, i.e., compact and sparse configurations, may emerge, which depend mainly on initial lateral and longitudinal gap spacing, i.e., H and G_0, respectively. In the compact cases, when H is small, e.g., $H < 0.6$, in terms of cruising speed and efficiency, hydrodynamic advantages are found for both plates. In all sparse configurations, the propulsive performance of the leading plate is identical to that of the corresponding isolated one. The following short plate in the "long-short" (the longer in the front) sparse cases always takes hydrodynamic advantages in terms of cruising speed and efficiency. In the "short-long" (the shorter in the front) sparse cases, the follower's propulsive capacity is suppressed because the cruising speed and input power decrease significantly compared to its isolated case. The analyses of hydrodynamic force and corresponding potential energy show that the staggered sparse configuration with $H \in (0.4, 1.0)$ is more stable than that with other H. The "hydrodynamic drafting" analyzed here may shed some light on understanding the coordinated collective behaviors in biological and natural systems. *Published by AIP Publishing.*
https://doi.org/10.1063/1.5053662

I. INTRODUCTION

Coordinated behaviors of large numbers of objects moving through a fluid are ubiquitous in biological and natural systems. Hydrodynamic drafting is one of the fascinating phenomena in the aggregates in which the flow-mediated interaction plays a critical role. Of particular interest are the collections of actively moving bodies in a fluid with a high-Reynolds-number ($Re \sim 10^2$–10^6), such as fish schools[1] and bird flocks,[2] in which the long-lasting inertial effects lead to complex flow.

It is plausible that the individuals in group save on the energetic cost of locomotion from the hydrodynamic interaction. For example, the V formation may improve the efficiency of flying birds by favorable interactions with the up- and downwash of leading neighbors, particularly over long migratory routes.[3,4] Similarly, fish in schools are supposed to take advantage of the wakes shed by neighbors within the school, thus reducing the cost of locomotion.[1,5] Understanding the drafting in collective swimming and flying is challenging because of the complex flow-structure interactions.

The two-body system, which is the simplest individual-level schooling or flocking model, has been used to investigate the general principle of the collective orderly configuration and the grouping energy characteristic. Numerous studies have focused on the coupling performance of the two passively flapping bodies,[6,7] as well as actively flapping flags or hydrofoils.[8,9] In the studies, the individuals were held fixed in an oncoming flow. However, the individuals in real groups are free to adapt their gait so as to achieve an orderly configuration. Therefore, a self-propelled model is necessary for further studying collective dynamics. There are many self-propulsion models for micro-organism.[10,11] To mimic fish swimming or bird flying, a few simple self-propulsion models, such as an undulatory plate[12] or a flapping plate,[13] have been developed.

The studies on the collective dynamics of two self-propulsive plates have been carried out.[13–16] In the self-propelled model, there is a prescribed heave motion at the leading edge of each plate but whose longitudinal swimming is free.[17] Becker *et al.*[14] and Ramananarivo *et al.*[15] experimentally studied two self-propelled wings swimming in a tandem array. Becker *et al.*[14] have shown that arrays of flapping and self-propelled wings select slow or fast modes due to constructive or destructive wing-wake interactions, respectively. However, in the study the horizontal spacing between the two plates was fixed, which implies an imposed configuration.[14] Inspired by the work of Becker *et al.*,[14] Ramananarivo *et al.*[15] performed an experiment in which the two bodies are free to select their speed and gap spacing. The results have shown that collective locomotion in orderly formations at an enhanced cruising speed can emerge from flow interactions alone. The observation supports the Lighthill conjecture that "orderly patterns could arise passively from aero- or hydrodynamic interactions, without the need for collective decision making or active control mechanisms."[15,18]

Zhu *et al.*[13] numerically studied the free locomotion of two self-propelled flapping filaments in a tandem configuration. They have shown that multiple stable configurations can

[a)]Author to whom correspondence should be addressed: huanghb@ustc.edu.cn

be spontaneously formed due to the vortex-body interaction and the energetic advantage was also observed in some emergent configurations. The multiple equilibrium configurations were confirmed by the experimental results.[15] To some extent, these studies supported the perspective of the Lighthill conjecture for the two-body system. Moreover, Peng *et al.*[16] studied the collective locomotion of two self-propelled flapping plates initially in a side-by-side arrangement. They showed that in view of hydrodynamics, to achieve higher performance the compact in-phase staggered-following mode and antiphase flappings in the side-by-side configuration are preferred.

The above observations are all based on the swimmers with identical propulsive capacity. It is not difficult to imagine that the swimmers may be easier to swim in the same gait and form equilibrium states with a uniform cruising speed. However, if the two plates have different propulsive capabilities, e.g., two plates have different flexibilities, it is unknown whether equilibrium configurations would emerge. We also would like to know whether and to what extent the Lighthill conjecture is valid under the circumstances and the propulsive performance of each plate in the school.

In the literature, the size effect on the collective patterns has been carried out.[19,20] Using an individual-based model of schooling agents, Hemelrijk and Kunz[19] found that in a group consisting of different sizes of individuals, some equilibrium spatial configurations emerge. However, the hydrodynamic interactions among school are simply modeled by artificial rules and not resolved physically.[19] Weihs[20] studied analytically forces and moments around a pair of unequally sized dolphin-like slender bodies, which are fixed in a uniform flow, to understand the inherent hydrodynamic drafting mechanism of a mother-calf pair of dolphins. The study has shown that in an ideal condition, drafting force can counteract a large part of the drag experienced by a neonate calf. Tian *et al.*[21] numerically studied the swimming performance and vorticity structures of two fish-like foils with different sizes in a flow. It is found that both foils benefit from tandem and staggered arrangements, by enhancing a reverse Kármán street or diminishing a Kármán street. However, the two bodies are fixed in Ref. 20 and the foils are not self-propelled in Ref. 21. In a word, the collective locomotion of two self-propelled swimmers with different propulsive capacities has never been investigated.

The self-propelled swimmers in collective locomotion are free to select their speed and relative position through flow-mediated interactions. Capturing this trait is essential to understand the hydrodynamic mechanisms of drafting in the emergent schooling patterns. Here, to further verify the Lighthill conjecture, two different self-propelled plates initially in a tandem or staggered configuration were studied. The effects of initial configurations, ratios of body length, as well as bending rigidity on the schooling dynamics and configurations, stability and propulsive performance are investigated systematically. To our knowledge, the collective behavior of two self-propelled plates with different propulsive capacities has never been studied.

This paper is organized as follows. The physical problem and mathematical formulation are presented in Sec. II. The numerical method and validation are described in Sec. III. Detailed results and discussion are given in Sec. IV, and concluding remarks are addressed in Sec. V.

II. PHYSICAL PROBLEM AND MATHEMATICAL FORMULATION

The schematic diagram of a self-propelled system consisting of two flapping flexible plates in a tandem ($H = 0$) or staggered ($H \neq 0$) configuration is shown in Fig. 1. The lateral and longitudinal distances between them are H and D, respectively. The plates with different lengths are immersed in a stationary viscous incompressible fluid initially. The leading edges of both plates are forced to heave sinusoidally in phase with an identical frequency f in the lateral direction. The forced lateral motions of the leading edges are prescribed by

$$y_1(t) = A_1 \cos(2\pi f t), \;\; y_2(t) = A_2 \cos(2\pi f t), \tag{1}$$

with zero active pitching angle, where A_1, A_2 are flapping amplitudes and here only $A_1 = A_2 = A$ is considered. The plates are unconstrained in the horizontal direction, and thus the inner spacing in the school may be dynamically selected as a result of flow-mediated coupling between the plates. The gap spacing between the plates is denoted by G. We have $G = D - L_1$. The initial gap spacing is denoted by G_0.

In this system, the fluid flow is governed by the incompressible Navier-Stokes equations,

$$\frac{\partial \boldsymbol{v}}{\partial t} + \boldsymbol{v} \cdot \nabla \boldsymbol{v} = -\frac{1}{\rho}\nabla p + \frac{\mu}{\rho}\nabla^2 \boldsymbol{v} + \boldsymbol{f}_b, \tag{2}$$

$$\nabla \cdot \boldsymbol{v} = 0, \tag{3}$$

where $\boldsymbol{v}$ is the velocity, p is the pressure, ρ is the density of the fluid, μ is the dynamic viscosity, and $\boldsymbol{f}_b$ is the body force term. The deformation and motion of the plates are described by the structural equation,[22,23]

$$\rho_l \frac{\partial^2 \boldsymbol{X}}{\partial t^2} - Eh\frac{\partial}{\partial s}\left[\left(1 - \left|\frac{\partial \boldsymbol{X}}{\partial s}\right|^{-1}\right)\frac{\partial \boldsymbol{X}}{\partial s}\right] + EI\frac{\partial^4 \boldsymbol{X}}{\partial^4 s} = \boldsymbol{F}_s, \tag{4}$$

where s is the Lagrangian coordinate along the plates, $\boldsymbol{X}(s,t) = (X(s,t), Y(s,t))$ is the position vector of the plates, $\boldsymbol{F}_s$ is the Lagrangian force exerted on the plates by the surrounding fluid, and ρ_l is the structural linear mass density. Eh and EI are the structural stretching and bending rigidity, respectively.

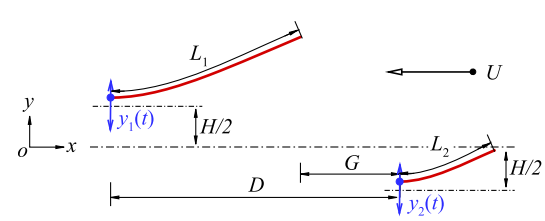

FIG. 1. Schematic diagram for a self-propelled system consisting of two flapping flexible plates in a tandem ($H = 0$) or staggered ($H \neq 0$) configuration. The longitudinal distance between the leading edges of the two plates is denoted by D, and the gap spacing between the plates is denoted by $G = D - L_1$. When the leading edges are forced to heave vertically and sinusoidally at their equilibrium positions, the plates deform passively and move in the horizontal direction freely. The schooling patterns may emerge spontaneously due to hydrodynamic interactions within the system.

For each plate, the horizontally unconstrained condition, vertical location due to the forced oscillation and the clamped condition are enforced at the leading edge ($s = 0$), i.e.,

$$-Eh(1 - |\partial \boldsymbol{X}/\partial s|^{-1})\partial X/\partial s + EI\partial^3 X/\partial^3 s = 0, \quad Y(t) = y(t), \quad \partial \boldsymbol{X}/\partial s = (1, 0). \tag{5}$$

The natural free-end boundary condition is imposed at the trailing edge ($s = 1$), i.e.,

$$-Eh(1 - |\partial \boldsymbol{X}/\partial s|^{-1})\partial \boldsymbol{X}/\partial s + EI\partial^3 \boldsymbol{X}/\partial^3 s = 0, \quad \partial^2 \boldsymbol{X}/\partial s^2 = 0. \tag{6}$$

There are two initial conditions for each plate, i.e., initial position $\boldsymbol{X}(s, 0) = \boldsymbol{X}_0(s)$ and initial velocity $\frac{\partial \boldsymbol{X}(s,0)}{\partial t} = (0, 0)$, where the initial position $\boldsymbol{X}_0(s) = (\frac{D_0 \mp D_0}{2} + s, \pm\frac{H}{2})$ is determined by D_0 ($D_0 = G_0 + 1$) and H.

The characteristic quantities ρ, L, and U_{ref} are chosen to normalize the above equations. The characteristic length is $L = min\{L_1, L_2\}$, and the characteristic velocity U_{ref} is the maximum flapping velocity of the plunging motion, i.e., $U_{ref} = 2\pi Af$. The dimensionless governing parameters are described as follows: the Reynolds number $Re = \rho U_{ref} L/\mu$, the stretching stiffness $\Gamma = Eh/\rho U_{ref}^2 L$, the bending stiffness $K = EI/\rho U_{ref}^2 L^3$, the mass ratio of the plates and the fluid $M = \rho_l/\rho L$, the heaving amplitude A, the lateral spacing H, and the initial gap spacing G_0. The subscripts "1" and "2" denote the parameters of plates 1 and 2, respectively. For example, K_1 and K_2 are the bending stiffness of plates 1 and 2, respectively. In the following discussions, all the parameters are nondimensionalized, e.g., H, D, G, A are normalized by L, unless otherwise specified.

III. NUMERICAL METHOD AND VALIDATION

The governing equations of the fluid-plate problem are solved numerically by the lattice Boltzmann method (LBM) for the fluid flow and a finite element method for the deformation of the flexible plates. The immersed boundary (IB) method is applied to treat the flow-structure interaction.[24,25] The body force term $\boldsymbol{f}_b$ in Eq. (2) represents an interaction force between the fluid and the immersed boundary to enforce the no-slip velocity boundary condition. Equation (4) for the plate is discretized by a finite element method, and the deformation with large-displacement of the plate is handled by the corotational scheme.[27] A detailed description of the numerical method can be found in our previous papers.[23,28]

The lattice Boltzmann equation with the body force model[26] is employed to solve the viscous fluid flow

$$g_i(\boldsymbol{x} + \boldsymbol{e}_i\Delta t, t + \Delta t) - g_i(\boldsymbol{x}, t) = -\frac{1}{\tau}[g_i(\boldsymbol{x}, t) - g_i^{eq}(\boldsymbol{x}, t)] + \Delta t R_i, \tag{7}$$

where τ is the non-dimensional relaxation time associated with fluid viscosity, Δt is the time increment, and $g_i(\boldsymbol{x}, t)$ is the distribution function for particles with velocity $\boldsymbol{e}_i$ at position $\boldsymbol{x}$ and time t. The equilibrium distribution function g_i^{eq} and the forcing term R_i[29] are defined as

$$g_i^{eq} = \omega_i \rho\left[1 + \frac{\boldsymbol{e}_i \cdot \boldsymbol{v}}{c_s^2} + \frac{\boldsymbol{v}\boldsymbol{v} : (\boldsymbol{e}_i\boldsymbol{e}_i - c_s^2\boldsymbol{I})}{2c_s^4}\right], \tag{8}$$

$$R_i = (1 - \frac{1}{2\tau})\frac{1}{\rho c_s^2}\boldsymbol{f}_b \cdot (\boldsymbol{e}_i - \boldsymbol{v})g_i^{eq}, \tag{9}$$

where ω_i is the weighting factor and c_s is the speed of sound. The variables' velocity $\boldsymbol{v}$ and mass density ρ can be obtained by the distribution functions

$$\rho = \sum_i g_i, \tag{10}$$

$$\rho\boldsymbol{v} = \sum_i \boldsymbol{e}_i g_i + \frac{1}{2}\boldsymbol{f}_b \Delta t. \tag{11}$$

In the IB scheme, the Lagrangian force $\boldsymbol{F}_s$ in Eq. (4) can be calculated by the penalty method,[24,25]

$$\boldsymbol{F}_s(s, t) = \alpha \int_0^t [\boldsymbol{V}_f(s, t') - \boldsymbol{V}_s(s, t')]\mathrm{d}t' + \beta[\boldsymbol{V}_f(s, t) - \boldsymbol{V}_s(s, t)], \tag{12}$$

where α and β are penalty parameters which are selected based on the previous studies,[23] $\boldsymbol{V}_s = \frac{\partial \boldsymbol{X}(s)}{\partial t}$ is the plate velocity and $\boldsymbol{V}_f$ is the fluid velocity at the Lagrangian position $\boldsymbol{X}$, which is obtained by interpolation

$$\boldsymbol{V}_f(s, t) = \int \boldsymbol{v}(x, t)\delta(\boldsymbol{x} - \boldsymbol{X}(s, t)]\mathrm{d}\boldsymbol{x}. \tag{13}$$

In the IB scheme, the body force $\boldsymbol{f}_b$ on the Eulerian points can be obtained from the Lagrangian force $\boldsymbol{F}_s$ using the Dirac delta function, i.e.,

$$\boldsymbol{f}_b(x, t) = -\int \boldsymbol{F}_s(s, t)\delta(\boldsymbol{x} - \boldsymbol{X}(s, t)]\mathrm{d}s. \tag{14}$$

Based on our convergence studies with different computational domains, the computational domain for fluid flow is chosen as $(D + 50) \times 40$ in the x and y directions (see Fig. 1). The domain is large enough so that the blocking effects of the boundaries are very weak. A far-field boundary condition is imposed at upper and lower boundaries. Specifically, a constant pressure boundary is imposed.[30] Meanwhile, the lateral dimension is large enough to ensure that the velocity on the boundaries is close to zero. For the inlet and outlet boundaries, an identical constant pressure is imposed and $\partial \boldsymbol{v}/\partial x = 0$, i.e., numerical first order extrapolation of $\boldsymbol{v}$ is applied.[31] At the initial time, the fluid is stationary with zero velocity in the entire computational domain. In the x and y directions, the mesh is uniform with spacing $\Delta x = \Delta y = 0.01$. The time step is $\Delta t = T/10\,000$ for the simulations of fluid flow and plate deformation, where $T = 1/f$ is the flapping period. Moreover, a finite moving computational domain[23] is used in the x direction to allow the plates to move for a sufficiently long time.

The numerical strategy used in this study has been validated and successfully applied to a wide range of flows, such as the locomotion of a flapping flexible plate,[23] the dynamics of fluid flow over a circular flexible plate,[28] and the vorticity dynamics of fluid flow over a flapping plate.[32]

IV. RESULTS AND DISCUSSION

A. "Long-short" tandem cases ($H = 0$)

For two plates having different propulsive capacities, here plates with different lengths and bending stiffnesses are considered. In all of our simulations, the Reynolds number $Re = 200$ and the stretching stiffness $\Gamma_1 = \Gamma_2 = 1000$ are fixed. The stretching stiffness is large enough that the stretching deformation can be neglected.

First we consider two tandem plates with different lengths. Specifically, the leading plate is two times longer than the following one, i.e., $L_1 = 2L_2$. Here the characteristic length is $L = L_2$. It is noticed that the self-propelled performance of an isolated longer plate may be different from that of an isolated shorter one.[23,33] To determine the bending stiffness in the "long-short" case, at the beginning the self-propelled performance of an isolated plate is investigated. For the isolated shorter plates, the normalized length is $L_2' = 1$ and the key parameters are chosen to be $A_2 = 0.5$, $M_2 = 0.2$, which are consistent with those in the literature.[13,16] For the longer plate, the normalized length is $L_1' = 2$ and the key parameters $A_1 = 0.5$ and $M_1 = 0.4$ are fixed. It is noted that if the characteristic length is chosen to be L_1 instead of L_2, the corresponding mass ratio is $M_1 = 0.2$.

Figure 2 shows the cruising speed and efficiency of an isolated plate as functions of bending stiffness K. Here the cruising speed of the plate is defined as the averaged forward speed at the equilibrium state, i.e., $U = \int_0^T u(t)\mathrm{d}t/T = \int_0^T |\partial_t X(0,t)|\mathrm{d}t/T$, where $u(t)$ is the instantaneous horizontal speed of the plate. The propulsive efficiency $\eta = \frac{1}{2}MU^2/W$, where the input work W is computed as a time integral of the input power P required to produce the oscillation and the forward movement,[13,23] i.e., $W = \int_0^T P(t)\mathrm{d}t = -\int_0^T \int_0^1 \boldsymbol{F}_s(s,t) \cdot \partial_t \boldsymbol{X}(s,t)\mathrm{d}s\mathrm{d}t$. It is seen from Fig. 2(a) that $K = 1.0$ and $K = 14$ are optimum bending stiffnesses for the shorter and longer plates to achieve their highest cruising speed, respectively. Actually, numerous experimental and analytical studies[34–36] on the flapping flexible wing and plate also have shown that a proper flexibility may enhance the thrust of the plate. The cruising speed of the propulsive plate may be directly relevant to the thrust experienced by the plate in one flapping cycle.[34,36] When the plate is very flexible (e.g., $K = 0.1$ for $L' = 1$), the plate is subjected to a large bending deformation. However, the normal force which is perpendicular to the local segment of the plate, and therefore the thrust experienced by the plate are very small due to the compliance of the plate. When the plate is stiff (e.g., $K = 10$ for $L' = 1$), although the plate may be subjected to a larger normal force, the contribution of the normal force to the thrust is still small because the deformation of plate is small and the corresponding projection of the normal force to the horizontal direction is small. From Fig. 2(b), it is seen that the efficiency of the longer plate with $K = 14$ is almost identical to that of the shorter plate with $K_2 = 1.0$. Because the shorter and longer plates achieve their highest cruising speeds at $K_1 = 1.0$ and $K_2 = 14$, respectively, in the following study if it is not specified, $K_1 = 1$ and $K_2 = 14$ are fixed for the shorter and longer plates, respectively.

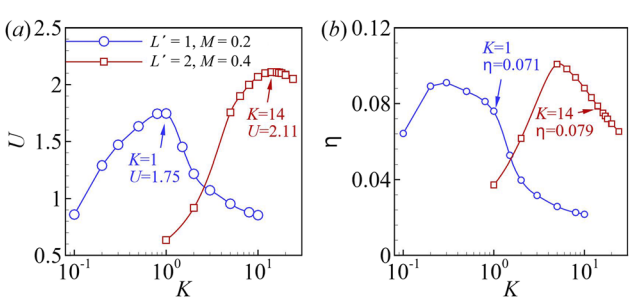

FIG. 2. Propulsive performance of an isolated plate: (a) cruising speed and (b) propulsive efficiency. For the shorter plate $L' = 1$ (normalized length) and $M = 0.2$. For the longer plate $L' = 2$ and $M = 0.4$. The other key parameters are $A = 0.5$, $Re = 200$, and $\Gamma = 1000$.

The key parameters in our simulations of "long-short" cases are listed in Table I. The tandem cases ($H = 0$) with different initial gap spacing G_0 were simulated. Two typical stable equilibrium configurations emerge spontaneously, i.e., compact and sparse configurations. Figures 3(a)–3(d) show the vorticity contours at four typical phases in one flapping cycle for the compact configuration. When G_0 is small, e.g., $G_0 = 1$, the compact configuration was observed. In the configuration, the shorter plate moves forward closely following the longer one. It is seen that in the compact configuration, the vorticity shedding from the trailing edge of the leader interacts and merges with the vorticity around the follower. The whole school behaves like a single and longer plate. The uniform cruising speed of the school is $U = 2.40$, which is larger than those of the isolated longer and shorter plates, i.e., $U_1 = 2.11$ and $U_2 = 1.75$, respectively. This result indicates that both plates are able to obtain performance enhancement from hydrodynamic interaction in the compact configuration.

When G_0 is large, e.g., $G_0 = 4$, the sparse configuration emerges. Figures 3(e)–3(h) show the vorticity contours at four typical phases in one flapping period for the sparse configuration. It is seen that the shorter plate follows the longer one with a larger equilibrium gap spacing. In the sparse configuration, the follower seems to swim in the reversed Kármán vortex street with $2S$ pattern, which is shed from the trailing edge of the leader. The uniform cruising speed of the school is $U = 2.11$, which is identical to that of the isolated longer plate (i.e., $U_1 = 2.11$) and larger than that of the isolated shorter plate (i.e., $U_2 = 1.75$). This result indicates that only a shorter follower can obtain performance enhancement from vortex-structure interaction in the sparse configuration.

The dynamics of the emergent configuration is shown in the following. Figure 4(a) shows the gap distance $G(t)$ as a function of time. It is found that for cases $G_0 = 1$ and $G_0 = 2$, after a few flapping cycles $G(t)$ evolves to an equilibrium state with $G \approx 0.2$, which corresponds to the compact configuration. For cases $G_0 = 3$, 4, 5, 6, and 7, $G(t)$ evolves to an equilibrium state with $G \approx 6.3$ after $t/T > 6$, which corresponds to the

TABLE I. The key parameters in the simulations.

Cases	L_1'	L_2'	K_1	K_2	A_1	A_2	M_1	M_2
Long-short	2	1	14	1.0	0.5	0.5	0.4	0.2
Short-long A	1	2	1.0	14	0.5	0.5	0.2	0.4
Short-long B	1	2	1.0	8	0.5	0.5	0.2	0.4

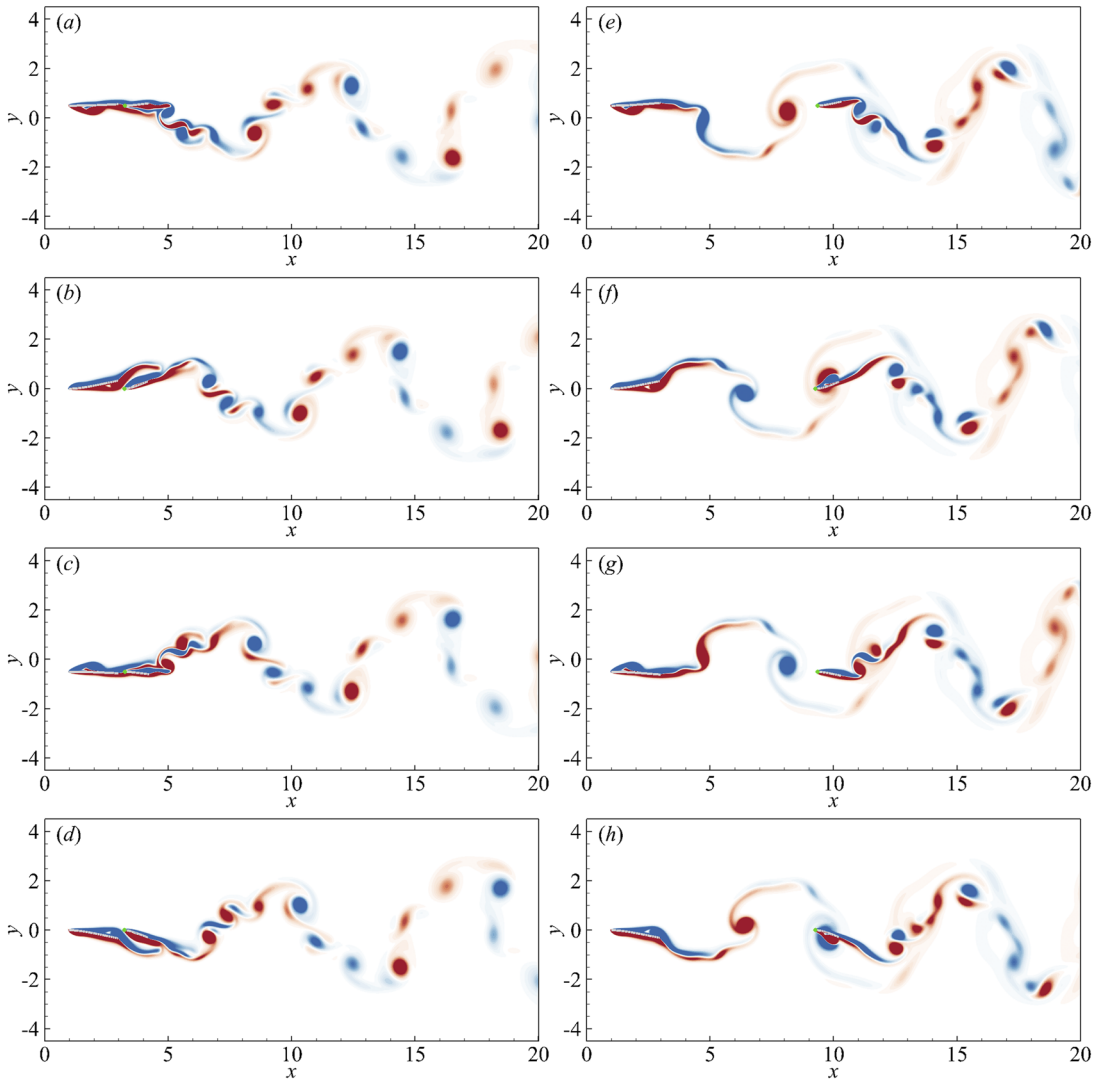

FIG. 3. Vorticity contours for the equilibrium compact (left column) and sparse (right column) configurations at four typical phases in one flapping cycle: [(a) and (e)] $t/T = 0$, [(b) and (f)] 1/4, [(c) and (g)] 2/4, and [(d) and (h)] 3/4. In the two "long-short" tandem cases, the initial gap spacings are $G_0 = 1$ (left column) and $G_0 = 4$ (right column). The leading edge of the trailing plate is denoted with a green dot to show its location more clearly.

sparse configuration. For cases $G_0 = 8$, 9, 10, 11, and 12, $G(t)$ also evolves to the sparse configuration with an equilibrium spacing $G \approx 13.0$. Hence, the emergent equilibrium configuration mainly depends on G_0. As shown in Fig. 4(a), the critical G_0 between the compact and sparse configurations is $G_0^c \approx 2.5$.

The schooling number S has been introduced to describe quantitatively the collective patterns of the two-wing system.[14,15] Here S is defined as $S = G/\lambda$, where $\lambda = U/f$ is the wavelength of the trajectory/path, which is determined by flapping frequency f and cruising speed U. Hence, λ is also the characteristic length of the wakes. Based on the definition of the schooling number, we can obtain from Fig. 4(a) the evolution of S in the 11 cases we simulated [see Fig. 4(b)]. It is seen that for a sparse configuration, S evolves to $S \simeq 1$ or 2. This phenomenon is similar to that observed in the collective locomotion of two identical plates.

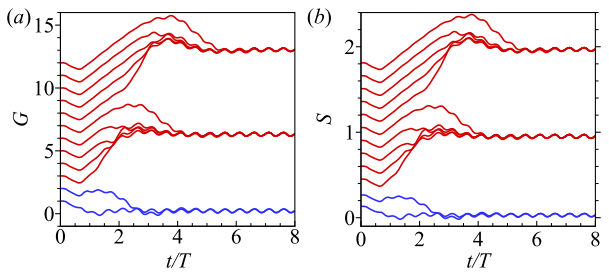

FIG. 4. Gap spacing G (a) and schooling number S (b) as functions of time for the "long-short" tandem cases. Each line represents a case we simulated.

Hence, here we can identify that in the compact configuration, cruising speeds of both plates are enhanced compared to their isolated cases. For the sparse configuration, the leading goose effect appears, i.e., cruising speed of the group U is identical to that of the leading one. Meanwhile, the cruising speed of the following one is enhanced.

B. "Short-long" tandem cases ($H = 0$)

In this section, we consider "short-long" cases, in which the longer plate follows the shorter one. The key parameters are shown in the row of "short-long A" in Table I. For all of the

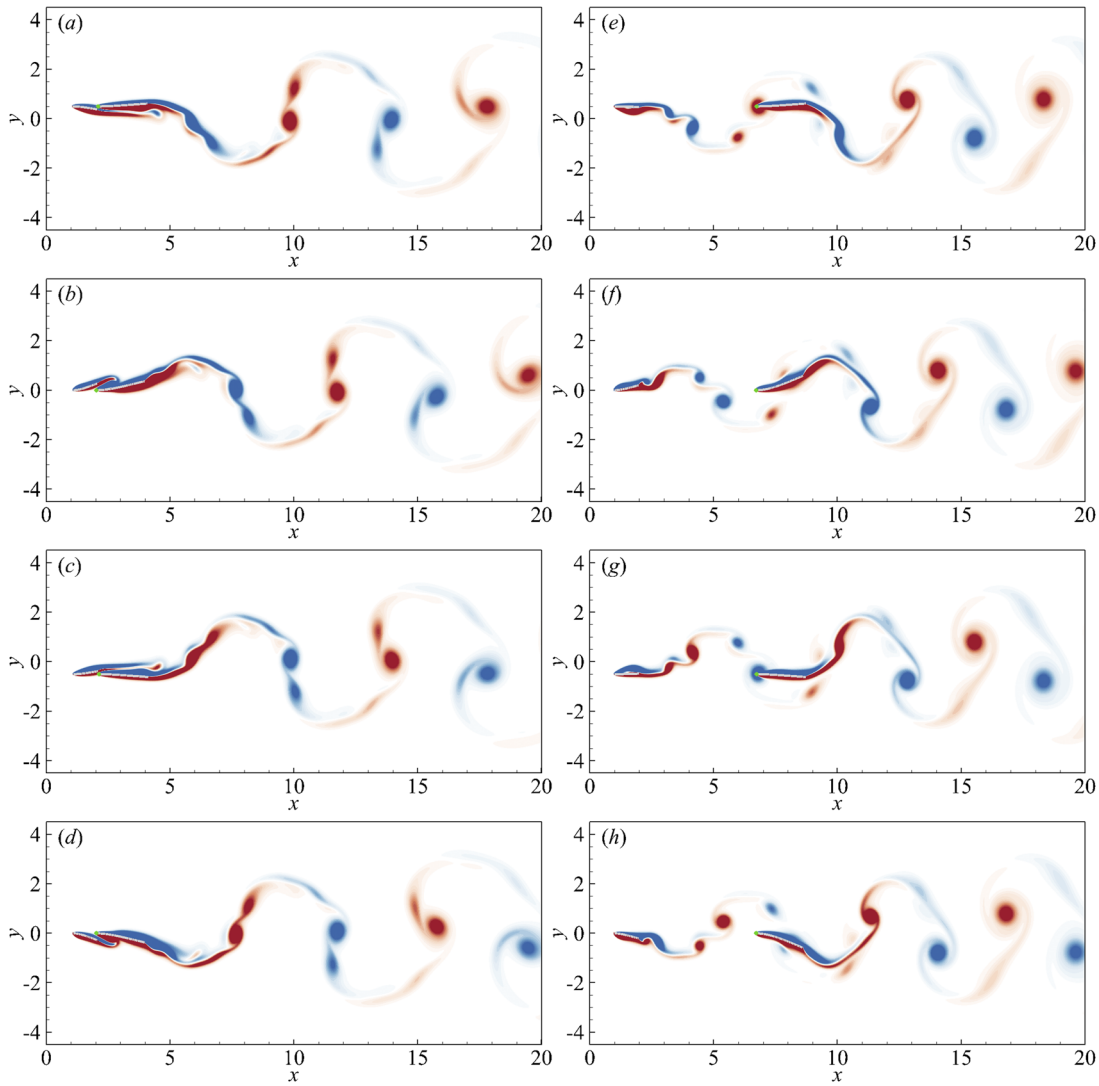

FIG. 5. Vorticity contours at four typical phases in one flapping cycle for compact (left column) and sparse (right column) configurations in the "short-long" tandem cases: [(a) and (e)] $t/T = 0$, [(b) and (f)] 1/4, [(c) and (g)] 2/4, and [(d) and (h)] 3/4. The parameters for the cases of left and right columns are listed in the second and third rows in Table I, respectively.

11 cases with $G_0 = 1, 2, 3, \ldots 11$, their equilibrium states are compact configuration as shown in the left column of Fig. 5 and sparse configurations are not observed. It may be understood as follows. The rear longer plate has a significantly stronger propulsive capacity; i.e., for the isolated setup, its cruising speed is significantly higher than that of the front plate. It may catch up the front one although it is not able to pass it due to the tandem setup. Figures 5(a)–5(d) show the vorticity contours at four typical phases in one flapping cycle for the compact configuration. It is seen that the shorter plate is close to the longer one. The whole school behaves like a single and longer plate with the "2*P*" vortex street shedding from the trailing edge of the follower. The vortex shedding pattern is different from that in the compact configuration in the "long-short" case. The uniform cruising speed of the collective locomotion is $U = 2.40$, which is identical to that in the "long-short" compact configuration. In this compact configuration, the propulsive speeds of the two plates are enhanced.

Table II shows the cruising speed of the emergent compact and sparse configurations for "long-short" and "short-long" cases. It is seen that in the compact configurations, the cruising speeds are enhanced for both plates compared to any isolated plate and the shorter one achieves a larger speed enhancement than the longer plate. In the sparse configurations, the cruising speed of the school is identical to that of the isolated leading plate. The leading plate looks like a leading goose in the collective locomotion. The following individual speeds up or slows down to compliant with the uniform gait.

TABLE II. Cruising speeds of compact and sparse configurations in "long-short" and "short-long" cases ($H = 0$). The speeds of isolated plates are also listed for comparison.

Emergent configurations	School	Isolated long plate	Isolated short plate
"Long-short" compact	2.40	2.11	1.75
"Long-short" sparse	2.11	2.11	1.75
"Short-long" compact	2.40	2.11	1.75
"Short-long" sparse	1.75	2.00	1.75

We have identified that for the "short-long" cases because the follower's propulsive capacity is significantly stronger, there are only compact configurations for cases with $G_0 < 12$. Here we weaken the following longer plate's capacity of self-propulsion by means of changing its bending stiffness to examine whether there is a sparse configuration. As shown in Fig. 2(a), for an isolated longer plate $L' = 2$, the cruising speed is $U \approx 2.0$ at $K = 8$, which is smaller than $U \approx 2.11$ at $K = 14$. As shown in Table I, in the cases of "short-long B," $K = 8$ is adopted. In this way, the sparse configurations emerge again in cases with a large G_0, e.g., $G_0 \geq 5$. Figures 5(e)–5(h) show the vorticity contours of the sparse configuration ($G_0 = 5$) at four typical phases in one flapping cycle. It is seen that the longer plate swims in the wake of the leading shorter plate with a large gap spacing between them, and the vortex shedding pattern is $2S$ mode instead of the $2P$ mode. In this "short-long" sparse configuration, the cruising speed of the school is identical to that of the isolated shorter plate ($U = 1.75$), and the following longer plate slows down due to the vortex-plate interaction compared to its isolated case.

C. Hydrodynamic benefit in "long-short" and "short-long" tandem cases

To fully evaluate the hydrodynamic advantages of the follower, the input power and efficiency are also calculated. The input powers and propulsive efficiencies for the compact and sparse configurations ($H = 0$) are shown in Tables III and IV, respectively. It is seen that in the sparse configurations, no matter "long-short" or "short-long" cases, the input power and efficiency of the leading plate are identical to its isolated case. In the "long-short" sparse configurations, the follower's input power is slightly larger than that of its isolated case. However, in the "short-long" sparse configuration, the follower's input power decreases compared to that of its isolated case because its propulsive capacity is inhibited. It is also noted that in all sparse cases ($H = 0$), the efficiency of the follower is improved.

For the compact configurations, usually the input power of each plate in the school is increased compared to its isolated case, e.g., the "long-short" compact case. This is reasonable because usually more input power is required when kinetic energy of each isolated plate increases. However, it is also seen that in the "short-long" compact case, although the propulsive speed of the following long plate is enhanced, its input power P is reduced, compared to the isolated case. For the efficiency, each plate in the school cruises more efficiently than its isolated case due to the fluid-structure interaction.

Hence, in terms of cruising speed and efficiency, hydrodynamic advantages are found for both plates in the compact cases, no matter the "long-short" or "short-long" cases, and the following shorter plate in the "long-short" sparse cases.

TABLE III. Input powers in compact and sparse configurations ($H = 0$). The powers of isolated short and long plates are also listed for comparison. The power of the following plate is italicised.

	Schooling swimming		Isolating swimming	
Emergent configuration	Short plate	Long plate	Short plate	Long plate
"Long-short" compact	*1.76*	3.87	1.32	3.60
"Long-short" sparse	*1.35*	3.60	1.32	3.60
"Short-long" compact	1.73	*3.49*	1.32	3.60
"Short-long" sparse	1.32	*2.00*	1.32	2.71

TABLE IV. Propulsive efficiencies in compact and sparse configurations ($H = 0$). The efficiencies of the isolated short and long plates are also listed for comparison. The efficiency of the following plate is italicised.

	Schooling swimming		Isolating swimming	
Emergent configuration	Short plate (%)	Long plate (%)	Short plate (%)	Long plate (%)
"Long-short" compact	*10.4*	9.43	7.39	7.87
"Long-short" sparse	10.5	7.87	7.39	7.87
"Short-long" compact	10.5	*10.4*	7.39	7.87
"Short-long" sparse	7.39	*9.75*	7.39	9.40

D. Staggered configurations ($H \neq 0$)

Here we examine the possible equilibrium states of staggered configurations by introducing a lateral spacing H. The parameters are identical to the "long-short" cases listed in Table I. In our simulations, cases of $G_0 \in [1, 12]$ were investigated. In this small section, typical initial gap spacings $G_0 = 1$ and $G_0 = 4$ are adopted to make compact and sparse configurations appear, respectively. The dynamics of the emergent configuration for cases $G_0 = 1$ and $G_0 = 4$ is shown in Fig. 6. It is seen that when $t/T > 15$, the schooling number S is close to zero and unity for compact and sparse configurations, respectively.

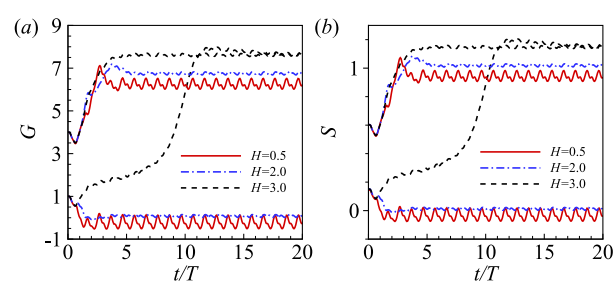

FIG. 6. Evolution of G (a) and S (b) with varying H for the "long-short" staggered cases.

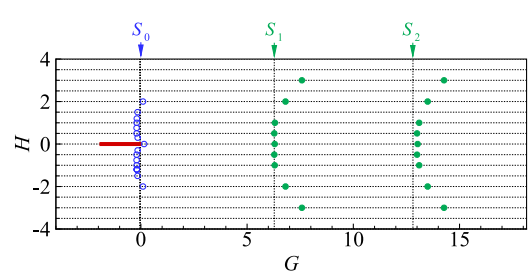

FIG. 7. Emergent equilibrium configurations in the G–H plane for "long-short" cases. Each circle (hollow or filled) in the plane represents a case we simulated. The solid red line represents the long plate. Its trailing edge is located at $(G, H) = (0, 0)$. The locations of the leading edge of the short plate for the compact and sparse configurations are denoted as hollow and filled circles, respectively. S_0, S_1, and S_2 represent the locations with $S \approx 0$, 1, and 2, respectively.

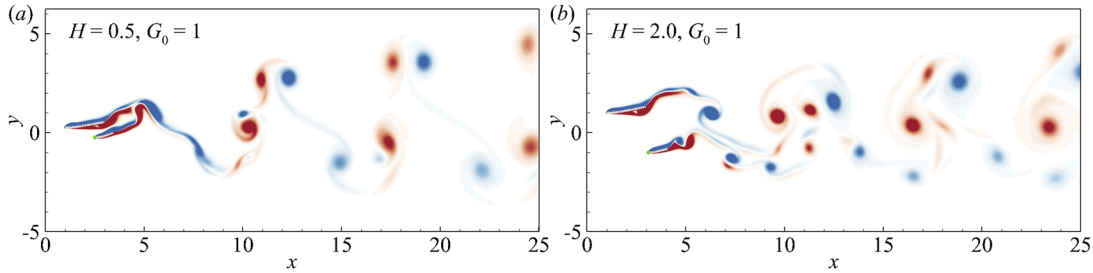

FIG. 8. Instantaneous vorticity contours for two compact configurations in the "long-short" staggered cases: (a) $H = 0.5$ and (b) $H = 2.0$. In the two cases, $G_0 = 1$.

Figure 7 shows the emergent stable configurations in the G–H plane. The red solid line denotes the longer plate, the trailing edge of which is located at $(G, H) = (0, 0)$. The locations of the leading edge of the short plate ($L'_2 = 1$) for the compact and sparse configurations are denoted by hollow and filled circles, respectively. Our results show that when $H \leq 2$, both compact and sparse configurations may emerge depending on G_0 (see Figs. 6 and 7). However, when the lateral spacing is large, e.g., $H = 3$, only the sparse configurations are formed spontaneously for all G_0. When H increases further, e.g., $H \geq 4$, the system seems not able to maintain an equilibrium configuration any more.

Figure 8(a) shows the instantaneous vorticity contours for $G_0 = 1$ and $H = 0.5$. It is seen that a compact staggered configuration with the shorter plate following the longer one appears. The vortices shedding from plates merge together immediately and evolve into an asymmetrical vortex street of $2P$ mode in the far field. Figure 8(b) shows the instantaneous vorticity contours for $G_0 = 1$ and $H = 2.0$. The two-plate system also spontaneously forms a compact staggered configuration. Due to the larger H, the wake shedding from each plate does not merge but interact together in the far field. More compact configurations can be found in Fig. 7 (see the hollow circles).

Moreover, when H and G_0 increase a little bit, sparse staggered equilibrium configurations may emerge (see the filled circles in Fig. 7). Figures 9(a), 9(c), and 9(e) show the instantaneous vorticity contours with $S \approx 1$ for the case of $G_0 = 4$, $H = 0.5$, 2.0 and 3.0, respectively. From Fig. 9(a), it is seen that when $H = 0.5$, the shorter plate always swims through

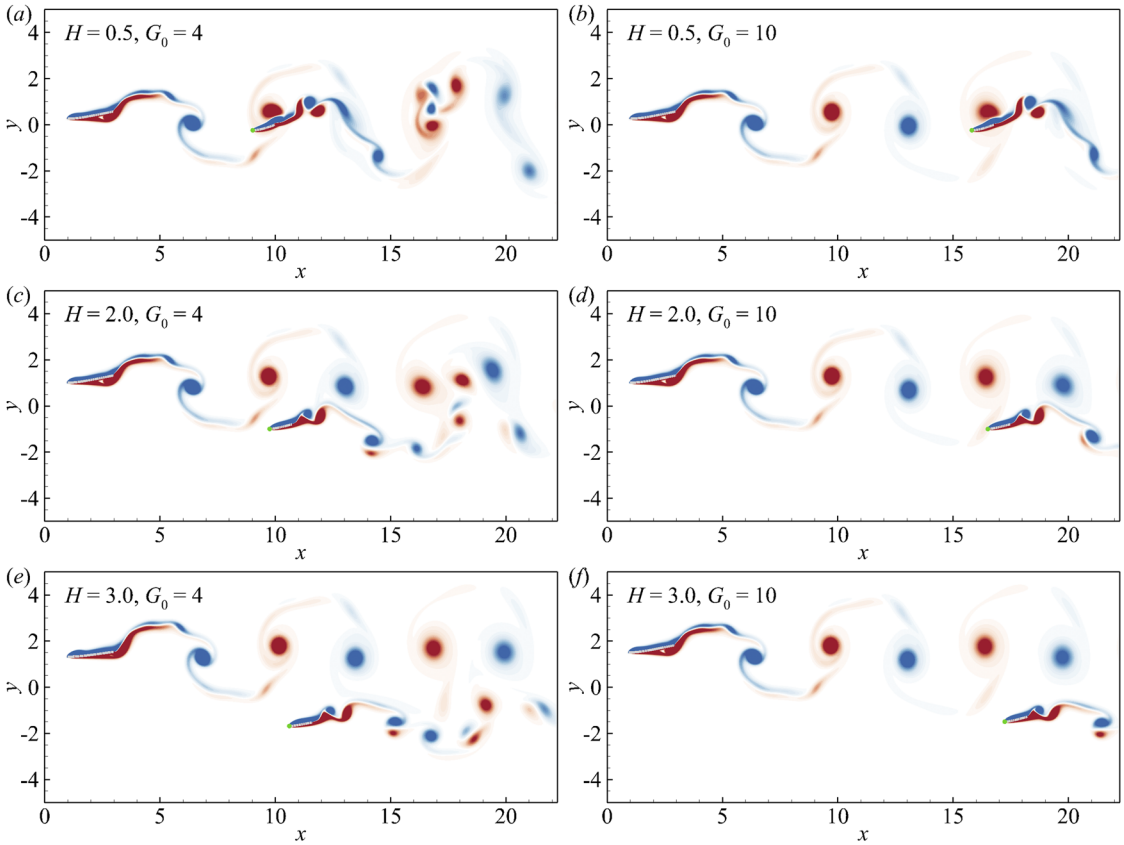

FIG. 9. Instantaneous vorticity contours for two sparse configurations in the "long-short" staggered cases: (a) $H = 0.5$, $G_0 = 4$; (b) $H = 0.5$, $G_0 = 10$; (c) $H = 2.0$, $G_0 = 4$; (d) $H = 2.0$, $G_0 = 10$; (e) $H = 3.0$, $G_0 = 4$; and (f) $H = 3.0$, $G_0 = 10$.

the vortex cores in the wake of the leader, and this pattern of plate-vortex interaction is also similar to that in tandem configurations [see Figs. 3(e)–3(h) and 5(e)–5(h)]. However, as H increases further, e.g., $H = 2.0$ or 3.0, the shorter plate swims on one side of the vortex street shed by the longer one and the trajectory of the follower does not go through the cores of oncoming vortices. Here this pattern of vortex-body interaction is referred to as vortex riding mode, by which the follower can also achieve a considerable performance enhancement (see Sec. IV G for details).

When G_0 becomes larger, e.g., $G_0 = 10$, the follower reaches another equilibrium location with the corresponding schooling number $S \approx 2$ (see the filled circles at $S^{eq} \approx 2$ in Fig. 7). The typical cases are shown in Figs. 9(b), 9(d), and 9(f). It is seen that the follower also adopts the vortex-riding mode to take advantages.

E. Schooling performance for staggered configurations

We have identified that "long-short" staggered cases may evolve spontaneously to discrete equilibrium schooling states with the schooling number $S \approx 0, 1, 2, \ldots$. To distinguish the emergent stable configurations, the compact configurations with $S \approx 0$ are referred to as the S_0 state, and sparse configurations with $S \approx 1, 2$ are referred to as S_1 and S_2 states, respectively. For the compact configurations, the shorter plates are close to the trailing edge of the longer plate (S_0). For the sparse configurations (S_1 and S_2 states), the location of the shorter plate slightly deviates downstream from the integer schooling numbers as H increases (see Fig. 7).

Figure 10(a) shows the cruising speed U as a function of H for the compact configurations (i.e., S_0). It is seen that as H increases, U reaches a peak at $H \approx 0.15$ and then decreases rapidly to the valley at $H \approx 1.2$. The follower achieves a considerable enhancement of cruising speed for all H compared to its isolated case. For the long leading plate, the speed enhancement is only achieved in cases with $H < 0.6$. It is noted that the emergent equilibrium configuration is the sparse one when $H = 3.0$, in which the cruising speed of the school is identical to that of the isolated long one.

Figure 10(b) shows the averaged power P as a function of H. It is seen that the powers consumed by both plates are larger than those of the isolated cases when $H < 1.0$. As H increases, the power P of the leader reaches a peak at $H \approx 0.2$ and then decreases and approaches a constant, while the power of the shorter follower reaches a valley at $H \approx 0.2$, which is close to that of the isolated short plate. In addition, it is seen that the overall system consumes most power at $H \approx 0.15$.

Figure 10(c) shows propulsive efficiency η as a function of H. It is seen that the overall efficiency of the school is larger than that of either isolated plate. The efficiency of the short plate is enhanced compared to its isolated case for all H we considered. However, for the leading plate, the efficiency enhancement is only achieved in cases with $H < 0.6$. Moreover, the enhancement of the shorter plate is more significant than that of the longer plate, e.g., the propulsive efficiencies of the long and short plates increase 67% and 10% at $H \approx 0.3$, respectively, compared to their isolated cases. This fact suggests that the short individual may harvest more hydrodynamic advantages from the "long-short" school.

The propulsive performance of the sparse configurations (e.g., S_1 and S_2) is discussed further. For the states S_1, S_2, the propulsive performances including the cruising speed, power, and efficiency of the longer leading plate are identical to those of an isolated one. Thus we only investigated the effect of flow interaction on the propulsive performance of the following plate. Figure 11(a) shows that the speed of the short follower is always identical to that of the leader. Thus the cruising speed of the shorter plate was enhanced compared to the isolated case due to the plate-wake interaction in school. Figures 11(b) and 11(c) show that the averaged power P and the efficiency η as functions of H for the S_1 and S_2 states. It is seen that the short plate consumes less power in the cases with smaller H, e.g., $H < 0.8$. It results in a higher efficiency at $H < 0.8$. For $H \leq 3$ investigated here, the efficiency is higher than that of the isolated case, which means the follower obtained hydrodynamic advantages from the plate-wake interaction.

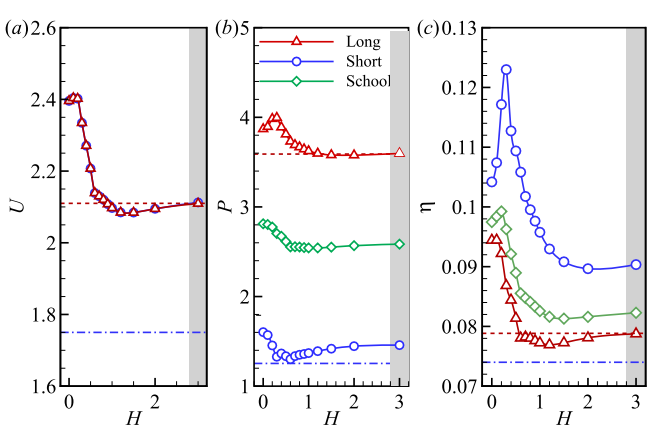

FIG. 10. Propulsive performance for (a) propulsive speed U, (b) averaged power P, and (c) propulsive efficiency η as functions of H for the compact "long-short" staggered configurations. Dashed and dashed-dotted lines denote the performance of the isolated longer and shorter plates, respectively. The equilibrium sparse configuration for $H = 3.0$ is marked with the gray region for comparison.

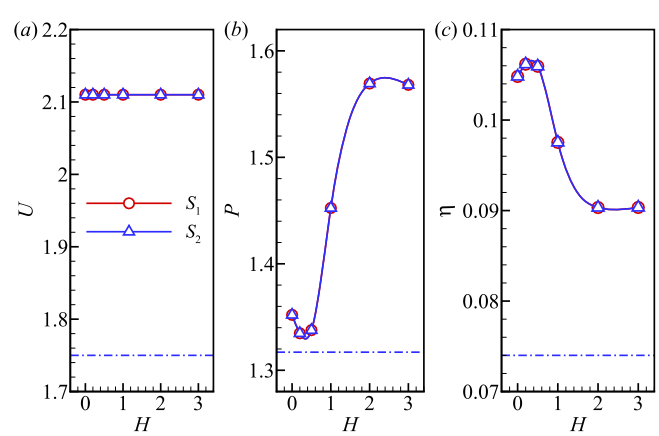

FIG. 11. Propulsive performance for (a) propulsive speed U, (b) averaged power P, and (c) propulsive efficiency η of the following short plate as a function of H for the sparse "long-short" staggered configurations (S_1, S_2). Dotted line denotes the propulsive performance of the isolated short plate.

TABLE V. Propulsive power P and efficiency η for the following long plate in the staggered sparse "short-long" configurations ($H \neq 0$) with $G_{eq} \approx 5.7$ and $U = 1.75$. P and η of the isolated long plate are also listed for comparison. The simulation parameters are listed in Table I ("short-long B") and the initial gap $G_0 = 8$.

H	P	η (%)
0.1	2.00	9.75
0.2	2.03	9.60
0.5	2.10	9.28
Isolated	2.71	9.40

We would also like to discuss the schooling performance of the staggered sparse "short-long" configurations ($H \neq 0$). It is found that when H is small and G_0 is large, staggered sparse "short-long" configurations would appear in the "short-long B" cases (see Table I for the parameters). The flow fields look like those in Fig. 3 ($H = 0$) and Fig. 9. The propulsive power and efficiency for the following long plate in the staggered sparse "short-long" configurations ($H \neq 0$) are shown in Table V. All these sparse staggered groups ($H = 0.1$, 0.2, 0.5) cruise with a uniform speed $U = 1.75$, which is identical to that of the leading short plate. From Table V, it is seen that when H is small, e.g., $H < 0.4$, the efficiency of the following long plate is higher than that of the isolated long plate. Meanwhile, the following long plate consumes less power compared to its isolated case. The improvement of the efficiency and less energy consumption may be due to the plate-wake interaction.

It is also noted that when H is large, e.g., $H = 1.0$, the initial following long plate would pass the short one and form the "long-short" compact configuration (see Fig. 8), in which the long plate leads the group. It can be understood in the following way. When H is large, the influence of the leading plate's wake on the rear long plate is minor. Meanwhile, there is enough lateral spacing for the initial rear long plate to pass the short one due to its stronger propulsive capacity.

F. Schooling cohesion in the sparse configurations

In the "long-short" cases, we have revealed that the shorter plate may be "locked" in the multiple stable locations by the wake of the longer plate. It hints that the hydrodynamic interaction plays a key role in maintaining the schooling stability. To map out the stability of the S_1 state, hydrodynamic forces on the short plate near the equilibrium locations were calculated. Here the simulations were performed in an inertial coordinate system. Suppose the uniform cruising speed of the school is U, in the simulations the oncoming flows around the fixed configurations have uniform longitudinal velocity U and the gap spacings are equal to those obtained by the self-propelled models. Figure 12(a) shows the net fluid force F_x as a function of G for $H \in [0, 3.0]$.

The locations where $F_x = 0$ correspond to the possible equilibrium positions of the follower, i.e., $G \approx 2.8$, 6.3, and 9.4, as shown in Fig. 12(a). However, at the equilibrium positions with $\mathrm{d}F_x/\mathrm{d}\widetilde{G} > 0$, e.g., $G \approx 2.8$, the short plate will be pulled away from these equilibrium positions by the fluid force if we make it slightly deviate from these positions. Therefore these

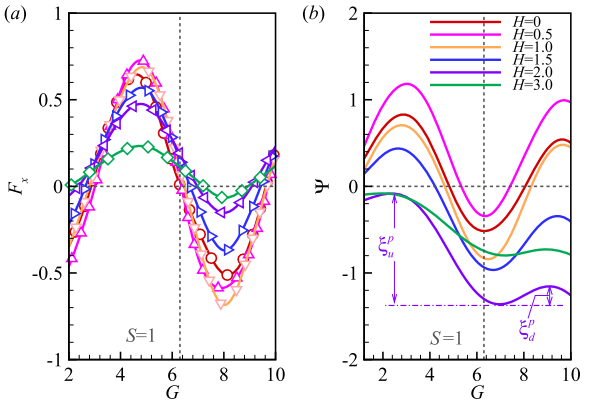

FIG. 12. Net fluid force F_x (a) and corresponding hydrodynamic potential $\Psi = -\int F_x dG$ (b) as functions of gap spacing G for the S_1 state. The well depths ξ_u^p and ξ_d^p for $H = 2.0$ are marked to illustrate their definitions.

locations are unstable and are not able to be observed in the simulations.

On the other hand, the locations where $F_x = 0$ and $\mathrm{d}F_x/\mathrm{d}\widetilde{G} < 0$ are stable equilibrium positions of the follower. For example, at $G \approx 6.3$, the fluid force acts as a restoring force, which is able to pull the slightly perturbed plate back to equilibrium positions. As shown in Fig. 12(a), the S_1 state predicted by the F_x–G profiles is consistent with that obtained from the numerical results (see Fig. 7).

In addition, the emergence of stable equilibrium positions may be illustrated in terms of a hydrodynamic potential, which is defined as the integral of force with respect to distance, i.e., $\Psi(G) = -\int F_x \mathrm{d}G$.[15] Figure 12(b) shows the hydrodynamic potential Ψ as a function of G for different H. It is found that there are well bottoms and peaks in the potential energy profiles, which correspond to the stable and unstable equilibrium states, respectively. This result indicates that the shorter follower always seeks the equilibrium locations with minimal potential energy in the wake of the leader through the flow-mediated interaction.

To further evaluate the tolerance of the stable state to flow perturbation, the well depths in the curves of $\Psi(G)$ are measured. As shown in Fig. 12(b) for the potential profile, there are two peaks in the upstream or downstream of the well bottom $S \approx 1$ for the case $H = 2.0$. The well depths can be measured from

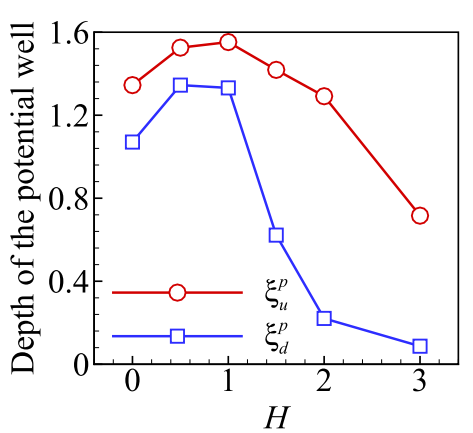

FIG. 13. Variation of the well depths ξ_u^p and ξ_d^p with H.

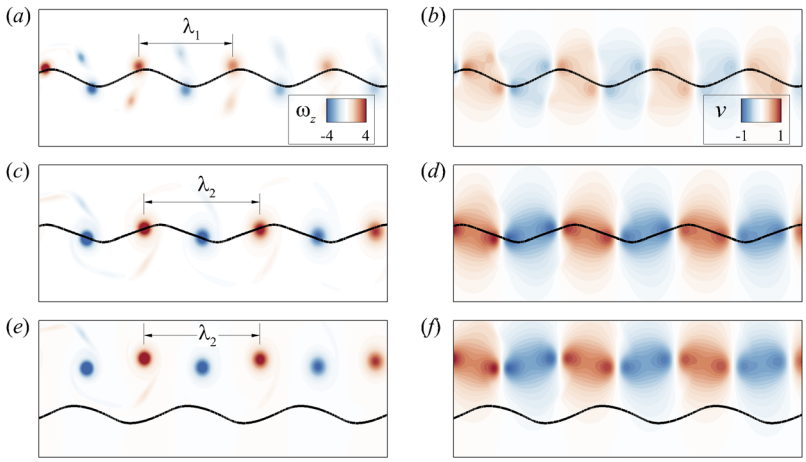

FIG. 14. Superimpositions of the leading-edge trajectories of the following plates in sparse configurations on the vorticity fields [(a), (c), and (e)] and vertical velocity fields [(b), (d), and (f)] generated by the leading plate in the corresponding isolated swimming. [(a) and (b)] The tandem "short-long" case, [(c) and (d)] the tandem "long-short" case, and [(e) and (f)] the "long-short" case with $H = 3.0$. The vortex-body interaction patterns are the interception mode [(a) and (c)] and the riding mode (e), respectively. λ_1 and λ_2 are the wavelengths of wakes of leading plates in "short-long" and "long-short" cases, respectively.

the upstream or downstream peaks, i.e., ξ_u^p or ξ_d^p, respectively. Taking case $H = 2.0$ as an example, ξ_u^p and ξ_d^p are marked in Fig. 12(b).

Figure 13 shows ξ_u^p and ξ_d^p as functions of H for the stable equilibrium state S_1. It is seen the variation trend of the two curves is consistent, i.e., they increase first and then decrease rapidly. ξ_u^p and ξ_d^p reach their peaks approximately in the region $H \in (0.4, 1.0)$. Hence, when $H \in (0.4, 1.0)$, the S_1 state is more stable than the S_1 state in the cases with other H. When H increases further, e.g., $H > 3.0$, the S_1 state may be difficult to maintain due to its low tolerance to flow perturbation.

G. Footprints of vortex-body interactions in the sparse configurations

The vortex-body interactions are important for understanding the mechanism of hydrodynamic benefits for a swimmer which encounters a vortical flow generated by the leader in school. Two typical patterns of vortex-body interactions have been found in the two-body systems,[9,13,37,38] i.e., vortex slalom mode and vortex interception mode. The slalom mode has been supposed to be an optimal trajectory in terms of drag reduction for a swimmer behind a flexible or rigid body in a uniform oncoming flow. In the mode, the swimmer slaloms between the vortex cores in the Kármán gait.[9,37,38] While for two self-propulsive plates, the following plate may adopt the interception mode to take energetic advantages. In the interception mode, the follower swims through the cores of the vortices in the reverse Kármán vortex street of the leader.[13]

To analyze the vortex-body interaction behavior in the emergent configurations, the superimpositions of the leading-edge trajectories of the following plates on the wakes of the leading isolated plates are shown in Fig. 14. For the tandem configurations ($H = 0$), it is seen that the interception mode is adopted by both "short-long" [Figs. 14(a) and 14(b)] and "long-short" [Figs. 14(c) and 14(d)] cases. Through locking itself in the oncoming vortices, the follower is able to follow the reverse Kármán gait generated by the leader. Similar mode can be found in Zhu *et al.*[13] and Uddin *et al.*[9]

As shown in Fig. 14(c), the wavelength of the shedding reverse Kármán vortices λ_2 is longer than λ_1 in Fig. 14(a). Since the follower is able to follow the reverse Kármán gait, it travels a longer distance (λ_2) within one flapping period in "long-short" configuration. In this way, the cruising speed of the follower is passively determined by the leader.

For the "long-short" case with $H = 3.0$, as shown in Figs. 14(e) and 14(f), the following plate moves forward with an enhanced speed by means of riding on one side of the oncoming reverse Kármán vortex street, i.e., the vortex riding mode. Hence, it is interesting to note that the advantage of this vortex riding mode in the reverse Kármán vortex street was first reported.

The restoring hydrodynamic force experienced by the follower near the equilibrium positions is critical in "locking" the follower's trajectory. The horizontal force F_x experienced by the follower as a function of time is shown in Fig. 15. The thrust can be evaluated by $T = (-|F_x| + F_x)/2$,[39] which is shown in gray in Fig. 15. The analysis result[15] has shown that the thrust on the follower due to the vorticity shed by the leader is proportional to the vertical velocity of the flow induced by the leader's wake. Hence, the force magnitude is supposed to be related to the wavy flow induced by the vorticity in the wake.[15,40]

From Fig. 15, it is seen that compared to the tandem "short-long" configuration, the follower in tandem "long-short" configuration experiences a larger thrust, due to the

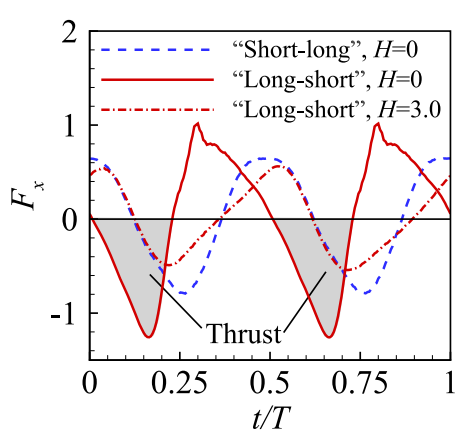

FIG. 15. Horizontal force F_x of the following plate for the typical configurations, i.e., the "short-long" case with $H = 0$ and "long-short" cases with $H = 0$ and 3.0. The thrust can be calculated by $T = (-|F_x| + F_x)/2$. As an example, the net thrust region for the "long-short" cases with $H = 0$ is marked by the gray color.

enhanced vertical flow induced by stronger vortices in the wake [see Figs. 14(b) and 14(d)]. Moreover, the thrust of the follower in the staggered "long-short" case ($H = 3$) is much smaller than that in the tandem "long-short" case because the induced vertical flow around the trajectory is weak [see Fig. 14(f)]. The corresponding schooling stability at $H = 3.0$ is worse than that of the tandem case (see Fig. 13).

In summary, in the sparse configurations, the hydrodynamic drafting or suppression of the follower arises depending on the wavelength of the oncoming wake behind the leader, while the schooling stability depends on the amplitude of vertical flow induced by the vorticity in the wake.

V. CONCLUSION

The collective locomotion of a pair of plates with comparable but different propulsive capacities is investigated numerically. The results show that for two flapping plates with different propulsive capacities, stable equilibrium configurations may emerge and they cruise with a uniform speed. It is also noted that stable equilibrium configurations may not appear if the propulsive capacity of one plate is much larger than that of the other.

Two typical equilibrium configurations are identified, i.e., compact and sparse configurations. The emergence of the equilibrium configurations depends mainly on initial lateral and longitudinal gap spacing, i.e., H and G_0. For tandem cases ($H = 0$), in terms of cruising speed and efficiency, hydrodynamic advantages are found for both plates in the compact cases, no matter the "long-short" or "short-long" cases. For staggered compact cases ($H \neq 0$), when H is small, e.g., $H < 0.6$, the issue of hydrodynamic advantages is identical to the tandem cases mentioned above. However, when H is large, cruising speed and efficiency of the long plate are slightly smaller than those of the isolated case.

In all sparse configurations, the propulsive performance of the leading plate is consistent with that of the isolated one. The following short plate in the "long-short" sparse cases always takes hydrodynamic advantages in terms of cruising speed and efficiency. For the "short-long" sparse cases, when H is small, the following long plate's efficiency is enhanced although its propulsive capacity is inhibited.

The hydrodynamic force and the corresponding potential energy in "long-short" sparse cases are analyzed for the following short plate in stable sparse state S_1 to reveal the stability of the state. The short follower is subject to a hydrodynamic restoring force near the stable equilibrium location, which maintains the schooling stability. The analysis of the well depths of the hydrodynamic potential profiles shows that the most stable S_1 state is the staggered sparse configuration with $H \in (0.4, 1.0)$.

Our results suggest that a plate with weak propulsive capacity may improve its propulsive performance by following a plate with strong propulsive capacity in the school. For two self-propulsive plates, besides the interception mode, the following plate may adopt vortex riding mode to take energetic advantages. A similar situation of hydrodynamic drafting in natural swimming school can be observed, such as dolphin drafting.[20] This study may shed some light on understanding the coordinated collective behaviors in biological and natural systems.

ACKNOWLEDGMENTS

This work was supported by the Natural Science Foundation of China (NSFC) (Grant Nos. 11872064 and 11621202). H.H. is supported by NSFC (Grant No. 11772326).

[1] D. Weihs, "Hydromechanics of fish schooling," Nature **241**, 290 (1973).
[2] S. J. Portugal, T. Y. Hubel, J. Fritz, S. Heese, D. Trobe, B. Voelkl, S. Hailes, A. M. Wilson, and J. R. Usherwood, "Upwash exploitation and downwash avoidance by flap phasing in ibis formation flight," Nature **505**, 399 (2014).
[3] P. B. S. Lissaman and C. A. Shollenberger, "Formation flight of birds," Science **168**, 1003 (1970).
[4] D. Hummel, "Aerodynamic aspects of formation flight in birds," J. Theor. Biol. **104**, 321 (1983).
[5] C. K. Hemelrijk, D. A. P. Reid, H. Hildenbrandt, and J. T. Padding, "The increased efficiency of fish swimming in a school," Fish Fish. **16**, 511 (2015).
[6] M. J. Shelley and J. Zhang, "Flapping and bending bodies interacting with fluid flows," Annu. Rev. Fluid Mech. **43**, 449 (2011).
[7] L. Zhu, "Interaction of two tandem deformable bodies in a viscous incompressible flow," J. Fluid Mech. **635**, 455 (2009).
[8] B. M. Boschitsch, P. A. Dewey, and A. J. Smits, "Propulsive performance of unsteady tandem hydrofoils in an in-line configuration," Phys. Fluids **26**, 051901 (2014).
[9] E. Uddin, W.-X. Huang, and H. J. Sung, "Actively flapping tandem flexible flags in a viscous flow," J. Fluid Mech. **780**, 120 (2015).
[10] S. Yazdi and A. Borhan, "Effect of a planar interface on time-averaged locomotion of a spherical squirmer in a viscoelastic fluid," Phys. Fluids **29**, 093104 (2017).
[11] G. Natale, C. Datt, S. G. Hatzikiriakos, and G. J. Elfring, "Autophoretic locomotion in weakly viscoelastic fluids at finite Péclet number," Phys. Fluids **29**, 123102 (2017).
[12] Z. Peng, O. S. Pak, and G. J. Elfring, "Characteristics of undulatory locomotion in granular media," Phys. Fluids **28**, 031901 (2016).
[13] X. Zhu, G. He, and X. Zhang, "Flow-mediated interactions between two self-propelled flapping filaments in tandem configuration," Phys. Rev. Lett. **113**, 238105 (2014).
[14] A. D. Becker, H. Masoud, J. W. Newbolt, M. Shelley, and L. Ristroph, "Hydrodynamic schooling of flapping swimmers," Nat. Commun. **6**, 8514 (2015).
[15] S. Ramananarivo, F. Fang, A. Oza, J. Zhang, and L. Ristroph, "Flow interactions lead to orderly formations of flapping wings in forward flight," Phys. Rev. Fluids **1**, 071201 (2016).
[16] Z.-R. Peng, H. Huang, and X.-Y. Lu, "Collective locomotion of two closely spaced self-propelled flapping plates," J. Fluid Mech. **849**, 1068 (2018).
[17] C. Zhang, H. Huang, and X.-Y. Lu, "Free locomotion of a flexible plate near the ground," Phys. Fluids **29**, 041903 (2017).
[18] M. J. Lighthill, *Mathematical Biofluiddynamics* (SIAM, 1975), Vol. 17.
[19] C. K. Hemelrijk and H. Kunz, "Density distribution and size sorting in fish schools: An individual-based model," Behav. Ecol. **16**, 178 (2004).
[20] D. Weihs, "The hydrodynamics of dolphin drafting," J. Biol. **3**, 8 (2004).
[21] F.-B. Tian, W. Wang, J. Wu, and Y. Sui, "Swimming performance and vorticity structures of a mother-calf pair of fish," Comput. Fluids **124**, 1 (2016).
[22] B. S. H. Connell and D. K. P. Yue, "Flapping dynamics of a flag in a uniform stream," J. Fluid Mech. **581**, 33 (2007).
[23] R.-N. Hua, L. Zhu, and X.-Y. Lu, "Locomotion of a flapping flexible plate," Phys. Fluids **25**, 121901 (2013).
[24] C. S. Peskin, "The immersed boundary method," Acta Numer. **11**, 479 (2002).
[25] R. Mittal and G. Iaccarino, "Immersed boundary methods," Annu. Rev. Fluid Mech. **37**, 239 (2005).
[26] S. Chen and G. D. Doolen, "Lattice Boltzmann method for fluid flows," Annu. Rev. Fluid Mech. **30**, 329 (1998).
[27] J. F. Doyle, *Nonlinear Analysis of Thin-Walled Structures: Statics, Dynamics, and Stability* (Springer, 2001).

[28]R.-N. Hua, L. Zhu, and X.-Y. Lu, "Dynamics of fluid flow over a circular flexible plate," J. Fluid Mech. **759**, 56 (2014).
[29]X. He, X. Shan, and G. D. Doolen, "Discrete Boltzmann equation model for nonideal gases," Phys. Rev. E **57**, R13 (1998).
[30]Q. Zou and X. He, "On pressure and velocity boundary conditions for the lattice Boltzmann BGK model," Phys. Fluids **9**, 1591 (1997).
[31]Z.-L. Guo, C.-G. Zheng, and B.-C. Shi, "Non-equilibrium extrapolation method for velocity and pressure boundary conditions in the lattice Boltzmann method," Chin. Phys. **11**, 366 (2002).
[32]G.-J. Li and X.-Y. Lu, "Force and power of flapping plates in a fluid," J. Fluid Mech. **712**, 598 (2012).
[33]L. Rosellini and J. Zhang, "The effect of geometry on the flapping flight of a simple wing" (unpublished), available at http://www.physics.nyu.edu/jz11/publications/LT10521stop.pdf.
[34]B. Thiria and R. Godoy-Diana, "How wing compliance drives the efficiency of self-propelled flapping flyers," Phys. Rev. E **82**, 015303 (2010).
[35]S. Ramananarivo, R. Godoy-Diana, and B. Thiria, "Rather than resonance, flapping wing flyers may play on aerodynamics to improve performance," Proc. Natl. Acad. Sci. U. S. A. **108**, 5964 (2011).
[36]R. C. Mysa and K. Venkatraman, "Intertwined vorticity and elastodynamics in flapping wing propulsion," J. Fluid Mech. **787**, 175 (2016).
[37]J. C. Liao, D. N. Beal, G. V. Lauder, and M. S. Triantafyllou, "Fish exploiting vortices decrease muscle activity," Science **302**, 1566 (2003).
[38]L.-B. Jia and X.-Z. Yin, "Passive oscillations of two tandem flexible filaments in a flowing soap film," Phys. Rev. Lett. **100**, 228104 (2008).
[39]R. G. Bottom II, I. Borazjani, E. L. Blevins, and G. V. Lauder, "Hydrodynamics of swimming in stingrays: Numerical simulations and the role of the leading-edge vortex," J. Fluid Mech. **788**, 407 (2016).
[40]T. Y. Wu and A. T. Chwang, "Extraction of flow energy by fish and birds in a wavy stream," in *Swimming and Flying in Nature* (Springer, 1975), pp. 687–702.